Biophysical Journal
Article

Biophysical Society

Release of Entropic Spring Reveals Conformational Coupling Mechanism in the ABC Transporter BtuCD-F

Marten Prieß[1] and Lars V. Schäfer[1,*]
[1]Center for Theoretical Chemistry, Faculty of Chemistry and Biochemistry, Ruhr-University, Bochum, Germany

ABSTRACT Substrate translocation by ATP-binding cassette (ABC) transporters involves coupling of ATP binding and hydrolysis in the nucleotide-binding domains (NBDs) to conformational changes in the transmembrane domains. We used molecular dynamics simulations to investigate the atomic-level mechanism of conformational coupling in the ABC transporter BtuCD-F, which imports vitamin B12 across the inner membrane of *Escherichia coli*. Our simulations show how an engineered disulfide bond across the NBD dimer interface reduces conformational fluctuations and hence configurational entropy. As a result, the disulfide bond is under substantial mechanical stress. Releasing this entropic spring, as is the case in the wild-type transporter, combined with analyzing the pairwise forces between individual residues, unravels the coupling mechanism. The identified pathways along which force is propagated from the NBDs via the coupling helix to the transmembrane domains are composed of highly conserved residues, underlining their functional relevance. This study not only reveals the details of conformational coupling in BtuCD-F, it also provides a promising approach to other long-range conformational couplings, e.g., in ABC exporters or other ATP-driven molecular machines.

INTRODUCTION

ATP-binding cassette (ABC) transporters are a large family of membrane protein complexes that couple the free energy gained from ATP binding and hydrolysis to the transport of substrate across the membrane, often uphill against a concentration gradient (1–6). ABC transporters are classified into importers and exporters. Exporters, which are present in both prokaryotes and eukaryotes, move substrates from the *cis*-side of the membrane (the side where ATP is bound and hydrolyzed) to the *trans*-side, i.e., in archaea and bacteria they move substrates out of the cell. By contrast, importers are only found in prokaryotes, where they mediate the uptake of nutrients. All ABC transporters have a core with the same architecture, a dimer of two nucleotide-binding domains (NBDs) and two transmembrane domains (TMDs). The NBDs are highly conserved among all ABC transporters, whereas TMDs can differ considerably. ATP is bound and hydrolyzed in the soluble NBDs to provide the free energy required for active transport, and the TMDs form the substrate transport pathway. Hence, the functional working cycle of ABC transporters involves coupling of ATP binding, hydrolysis, and product release in the NBDs to conformational changes in the TMDs, which ultimately switch in an alternating access manner between substrate accessibility from the *cis*- and *trans* sides of the membrane. It is an open question how exactly this allosteric cross talk (5) is accomplished. In particular, despite a growing number of available x-ray crystal structures, recently summarized in the review by ter Beek et al. (6), it remains to be elucidated in atomic detail 1) how the required tight coordination of interactions between the individual subunits is achieved, and 2) along which pathways the mechanical work is transmitted from the NBDs to the TMDs. In addition to this interest in ABC transporters from a mechanistic point of view, they are also of physiological importance. Malfunction of human ABC transport systems is linked to a plethora of diseases (7), and ABC exporters contribute to multidrug resistance of bacteria and cancer cells (8,9).

BtuCD from *Escherichia coli* is one of the structurally most thoroughly characterized ABC transporters (10–14). It is a type II importer comprising BtuC and BtuD homodimers that form the TMDs and NBDs, respectively. BtuCD facilitates the uptake of vitamin B_{12}, which is captured on the *trans*-side by the periplasmic substrate-binding protein BtuF that docks onto the core transporter (15). A distinct transport mechanism has been suggested (13,14) based on the available x-ray crystal structures, all of which represent static snapshots of different conformations along the proposed working cycle. These are 1) an ATP-bound BtuCD

Submitted February 10, 2016, and accepted for publication April 20, 2016.
*Correspondence: lars.schaefer@ruhr-uni-bochum.de
Editor: Jose Faraldo-Gomez.
http://dx.doi.org/10.1016/j.bpj.2016.04.027

outward-facing state (14), 2) an ATP-bound BtuCD-F occluded state (13), 3) a transient, inward-facing state that was deduced from the x-ray crystal structure of Hi1470/71 of *Haemophilus influenzae* (16), 4) a closed, asymmetric nucleotide-free BtuCD-F state (11), and 5) an outward-facing nucleotide-free BtuCD state (10). The mechanistic hypotheses have been corroborated by a wealth of functional assays (15,17,18) as well as by electron paramagnetic resonance spectroscopy (19–21), the latter with a particular focus on the gating mechanism in the TMDs. These studies also highlighted that ABC transporters with different TMD architecture, such as exporters and importers, or importers of type I and II, do not necessarily share the same mechanism (6).

Determination of high-resolution x-ray crystal structures of BtuCD (14) and BtuCD-F (13) in the nucleotide-bound state requires the reduction of residual ATPase activity and also the restriction of conformational dynamics. To trap the BtuD subunit in a closed sandwich conformation, Korkhov et al. (12) engineered an S-S bond that bridges the two BtuD chains across the NBD dimer interface by introducing the N162C mutation, in addition to the E159Q mutation that suppresses ATP hydrolysis. In this work, we used atomistic molecular dynamics (MD) simulations to investigate the effect of these mutations, as well as the presence or absence of ATP, on the structure and dynamics of BtuCD-F. Atomistic MD simulations are a powerful technique for studying the conformational dynamics of membrane protein systems (22,23) and have been applied to different ABC transporters, both for isolated NBD dimers in solution (24–35) and for entire transporter complexes in an explicit lipid membrane environment (36–47), also including BtuCD (48–52). While these initial efforts toward understanding the conformational transitions in BtuCD have elucidated important aspects, the atomic details of the mechanical coupling mechanism remain to be elucidated. To address this question, we carried out multimicrosecond MD simulations of the BtuCD-F complex embedded in a POPC lipid membrane (Fig. 1). We quantify how strongly, and in which structural elements, conformational fluctuations are reduced due to the engineered C162-C162 disulfide bond, which is found to be under substantial mechanical stress. Release of this entropic spring, combined with a spatially resolved analysis of interresidue forces, reveals a clear picture of the conformational coupling mechanism in terms of the pathways along which force is propagated from the NBDs to the TMDs. The residues involved in these identified networks are highly conserved, suggesting that they are of functional importance.

MATERIALS AND METHODS

MD simulations

All MD simulations were carried out with the GROMACS program package, ver. 4.6.5 (53,54). The BtuCD-F complex was simulated in a fully solvated

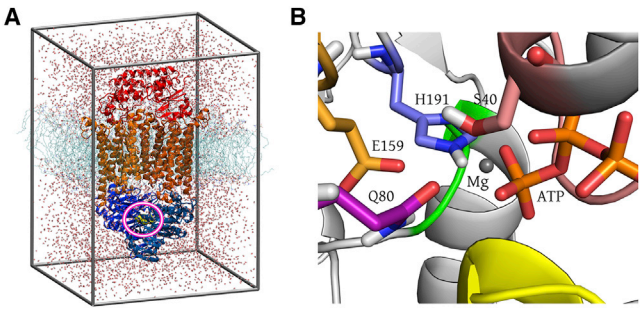

FIGURE 1 (*A*) MD simulation system. BtuCD-F is embedded in a solvated POPC bilayer. The subunits are colored blue (BtuD dimer), orange (BtuC dimer), and red (BtuF). The C162-C162 disulfide bond at the NBD dimer interface is highlighted. (*B*) The nucleotide binding site consists of the conserved motifs Walker A (*red*), Walker B (*orange*), Q-loop (*purple*), switch (*blue*), LSGGE (*yellow*), and D-loop (*green*). To see this figure in color, go online.

POPC (palmitoyloleoylphosphatidylcholine) lipid bilayer (Fig. 1). The simulations of the ATP-bound state were initiated from the x-ray crystal structure (PDB: 4FI3 (13)) after replacing AMP-PNP by ATP. The wild-type structure was obtained by changing glutamine 159 to glutamate and cysteine 162 to asparagine. For wild-type apo BtuCD-F, two sets of simulations were carried out (apo refers to the absence of ATP, not of vitamin B_{12}, which was not included in any of our simulations). The first set was initiated from the nucleotide-bound x-ray structure after removal of MgATP and reintroducing the wild-type residues E159 and N162. For the second set, we used the x-ray crystal structure of apo BtuCD-F (PDB: 2QI9 (11)). The first approach was adopted to generate a conformationally excited apo* state, and to probe by MD the onset of the relaxation toward the equilibrium apo state. The latter is, by construction, studied in the second set of simulations initiated from the actual apo x-ray crystal structure.

To determine the orientation and insertion of the protein in the lipid bilayer, the orientations of proteins in a membranes (OPM) web server (55) were used. The oriented protein was inserted into a preequilibrated POPC bilayer using the inflation/deflation protocol of Kandt et al. (56). The protein-bilayer systems were solvated such that no water molecules were introduced to the hydrocarbon region of the bilayer. The periodic simulation box contained BtuCD-F embedded in a bilayer comprised of 256 POPC lipids (128 in each leaflet), ~41,090 TIP4P-Ew (57) water molecules, and Na^+/Cl^- counterions to neutralize the simulation box. The *x*,*y*,*z* dimensions of the simulation box were ~11.0, 10.5, and 15.1 nm. The AMBER99SB-ILDN force field (58) was used for the protein. The protonation states of titratable side chains were assigned with PROPKA (59,60). For POPC, the Berger lipid parameters (61,62) were used, including dihedral parameters (63) for the torsion around the bond adjacent to the *cis* double bond in the POPC hydrocarbon tail. We used xLeap as part of the AMBER tools to create an ATP force-field topology, using the parameters from the AMBER99 force field for adenosine and the parameters published by Meagher et al. (64) for the triphosphate. Long-range electrostatic interactions were treated with the particle-mesh Ewald method (65) with a grid-spacing of 0.12 nm. Short-range van der Waals interactions were described with a Lennard-Jones 6-12 potential that was cut off at 1.0 nm. This cutoff was also used for the division between short- and long-range Coulomb interactions. The nonbonded neighbor list was updated every 20 fs. Analytical corrections to the pressure and potential energy were applied to compensate for the truncation of the Lennard-Jones interactions. The SETTLE algorithm (66) was used to constrain the bonds and angles of the water molecules, and LINCS (67) was used to constrain all other bond lengths. Together with virtual interaction sites for the protein hydrogen atoms (68), this allowed for an integration timestep of 4 fs. The temperature was kept constant at 300 K by coupling to a velocity rescaling thermostat (69) with a coupling time constant 0.4 ps. For constant pressure, semiisotropic coupling was

applied by separately coupling the lateral (x,y) and normal (z) directions to a pressure bath at 1 bar using a Berendsen barostat with a time constant of 2.0 ps and compressibility 4.5×10^{-5} bar^{-1}.

After energy minimization (1000 steps steepest descent), the system temperature was linearly raised from 60 to 300 K during 400 ps, followed by 20 ns equilibration at 300 K. During these simulations, harmonic position restraints with force constants 100 kJ mol^{-1} nm^{-2} were applied to all protein heavy atoms. Finally, for each system (apart from apo*), five independent 500-ns production MD simulations were carried out. Different random seeds were chosen for the initial Maxwell velocity distribution at 300 K. Because we studied five different systems (see Table 1), the overall simulation time accumulates to 12.5 μs.

Force on the disulfide bond

To obtain the force on the disulfide bond, we used the free energy implementation of GROMACS. We recorded the force acting on a constraint between the two disulfide S-atoms during the MD. The force is the negative gradient of the Hamiltonian with respect to the reaction coordinate λ, $F = -\partial H/\partial\lambda$. In our case, the reaction coordinate is the S-S bond length. A negative gradient (positive force) implies that the reaction coordinate tends to adopt larger values, i.e., a positive force represents a stretching (pulling) of the S-S bond. The relationship between the S-S bond distance, r, and the reaction coordinate used in the free energy implementation of GROMACS, λ, is $r(\lambda) = r_0 + \lambda \times (r_1 - r_0)$. Here, r_0 and r_1 are the bond lengths used for the initial ($\lambda = 0$) and final ($\lambda = 1$) states, respectively. The equilibrium length r_0 was set to 0.2038 nm, as defined in the force field. To obtain the desired force, the derivative of the Hamiltonian with respect to λ needs to be the physical force, i.e., $dH/d\lambda = dH/dr \times dr/d\lambda = dH/dr$. Thus, $dr/d\lambda = 1$. Therefore, because $dr/d\lambda = r_1 - r_0$, setting $r_1 = r_0 + 1$ nm directly yields the force on the S-S bond in units of kJ mol^{-1} nm^{-1}.

TABLE 1 Overview of Simulation Systems and Mean Cα-RMSD with Respect to Starting Structure, Averaged Over the Last 100 ns of Each MD Simulation

System	Simulation	Duration (ns)	Cα-RMSD (nm)
BtuCD-F•MgATP (E159Q/N162C)	mut1	500	0.161
	mut2	500	0.185
	mut3	500	0.172
	mut4	500	0.169
	mut5	500	0.182
BtuCD-F•MgATP (wild-type)	wt1	500	0.177
	wt2	500	0.159
	wt3	500	0.161
	wt4	500	0.169
	wt5	500	0.196
BtuCD-F•MgATP (wild-type, H191$^+$)	wt$^+$ 1	500	0.166
	wt$^+$ 2	500	0.168
	wt$^+$ 3	500	0.190
	wt$^+$ 4	500	0.167
	wt$^+$ 5	500	0.155
BtuCD-F apo (wild-type)	apo1	500	0.181
	apo2	500	0.182
	apo3	500	0.285
	apo4	500	0.191
	apo5	500	0.191
BtuCD-F apo* (wild-type)	apo*1	800	0.208
	apo*2	800	0.211
	apo*3	900	0.188

The apo* structure was generated by removing MgATP from the nucleotide-bound structure.

Configurational entropy

We calculated configurational entropies using the quasi-harmonic approximation as formulated by Schlitter (70). Following the procedure described previously in Baron et al. (71,72), Debnath and Schäfer (73), and Fisette et al. (74), we analyzed the entropy buildup over time. The quasi-harmonic approximation yields an upper bound to the configurational entropy, $S = 0.5\ k_B \ln\det(1 + k_B T e^2 \hbar^{-2}\ \mathbf{MC}) > S_{true}$. We are only interested in entropy differences between two states, ΔS, where the entropies of both states can be expected to be overestimated to a similar degree, and hence this effect to largely cancel-out. In the above formula, k_B is Boltzmann's constant, T is the temperature, e is Euler's number, $\hbar$ is the reduced Planck constant, and $\mathbf{M}$ is the 3N-dimensional diagonal mass matrix for the N particles. $\mathbf{C}$ is the covariance matrix of particle positions with the matrix elements $C_{ij} = \langle(\vec{x}_i - \langle\vec{x}_i\rangle)(\vec{x}_j - \langle\vec{x}_j\rangle)\rangle$, where $\vec{x}_i$ is the three-dimensional Cartesian coordinate vector of particle i. For removing overall translation and rotation, we used the starting structures of our MD simulations as reference structures for fitting. Averaging was done over all trajectory frames. Covariance analysis was carried out for fluctuations of Cα-atoms, either for the entire BtuCD-F complex, or for the individual dimeric BtuC, dimeric BtuD, and BtuF subdomains separately. This decomposition into the contributions from the individual subdomains neglects correlations between them (i.e., the entropy of the entire complex is not simply the sum of the entropies of the individual subdomains), but it enables us to assign changes in entropy to certain structural elements.

Force distribution analysis

Pairwise residue-residue forces in BtuCD-F were analyzed through force distribution analysis (75,76). Force distribution analysis (FDA) has been used previously to investigate the mechanics of different proteins in terms of stress (re-)distribution, with a focus also on allosteric communication (77–79) and protein-protein interactions (74). One advantage of FDA over analyzing correlated motions is that atomic displacements are often small, but can nevertheless lead to rather large forces. Using the GROMACS-PF2 ver. 4.5.3 implementation of FDA (80), we calculated the forces F_{ij} between atom pairs i,j for every frame of our MD trajectories. According to Newton's third axiom, in equilibrium, the sum of interatomic forces F_{ij} on any atom i is on average zero over time, $\langle\sum_j \vec{F}_{ij}\rangle = 0$. However, individual forces between pairs of atoms i and j (or, accordingly, pairs of residues v and w) do not necessarily need to average out to zero. We analyzed pairwise interresidual forces, which were calculated as the norm of the sum of all interatomic force vectors between all atoms i and j of residues v and w, $F_{vw}^{res} = \left|\sum_{ij}\vec{F}_{ij}\right|$, with $i \in v$, $j \in w$. Attractive and repulsive forces are distinguished by sign. Forces were averaged over the entire (accumulated) MD data to minimize statistical error. To analyze force differences between different forms of BtuCD-F, e.g., wild-type and disulfide mutant, we calculated the absolute differences of the interresidual forces, $\Delta F_{vw}^{res} = \left|F_{vw}^{res}(\mathrm{wt}) - F_{vw}^{res}(\mathrm{mut})\right|$. We interpret the degrees of freedom with large force differences ΔF_{vw}^{res} as pathways of the propagation of mechanical perturbations, see below. This is justified in our case, because for all BtuCD-F systems investigated in this work, the introduced perturbations can be considered relatively minor in relation to the size and complexity of the overall system (e.g., wild-type versus disulfide mutant, or ATP-bound versus -unbound state).

RESULTS AND DISCUSSION

Structural stability

We carried out several MD simulations of different BtuCD-F systems (Table 1). These include the ATP-loaded E159Q/N162C disulfide mutant used for crystallization (13,14), the

wild-type, and apo BtuCD-F (i.e., in the absence of nucleotide). First, we investigated the structural stability of the overall BtuCD-F complex (Fig. 1, 1389 residues) as well as of each subunit individually (BtuC, BtuD, BtuF). Table 1 shows the deviation of the protein from the starting structure for all simulations (see also Fig. S1 in the Supporting Material). For both wild-type (wt) and mutant, the Cα-root mean-square deviation (RMSD) of the entire transporter complex stabilizes at ~0.2 nm, reflecting a stable structure that undergoes thermal fluctuations in the vicinity of the starting structure.

Asymmetry of the NBDs

The NBDs are formed at the interface of chains A and B of the homodimeric BtuD subunit (Fig. 1). They contain highly conserved motifs that are essential for ATP binding and hydrolysis. First, we focus on the comparison of the ATP-bound form of wt and E159Q/N162C mutant; apo BtuCD-F will be discussed later. For the subsequent analysis, we use the following definition: NBD1/2 consists of Walker A, Walker B, Q-loop, and the H191/switch motif from monomer A/B, and the LSGGE and D-loop from monomer B/A. To investigate the overall structural integrity of these elements, Fig. 2 shows the RMSD distributions. In the E159Q/N162C mutant, the deviations of the NBDs from the starting structure are very small, as shown by the sharp distributions peaking at ~0.08 nm. By contrast, for the wt, the distributions are broader and shifted to slightly larger values, with peak positions at ~0.10 and 0.13 nm for NBD1 and NBD2, respectively. Thus, especially wt NBD2 deviates stronger from its starting structure. In addition, the tail of the distribution that extends up to 0.22 nm indicates a more heterogeneous structural ensemble. This difference in RMSD from the starting structure suggests a different time evolution of NBD1 and NBD2 during the MD, which would lead to asymmetric structures. To test this hypothesis, we calculated the RMSD after fitting NBD2 on NBD1 for each time frame of the simulation (Fig. 2 *B*). The x-ray structure (13) was solved with twofold noncrystallographic symmetry restraints (except from the parts that contact the asymmetric BtuF), and the structures of the two NBDs are hence very similar (Fig. 2 *B*, *black vertical line*). For the E159Q/N162C disulfide mutant, we find a mean RMSD of 0.08 nm, and thus only slightly asymmetric behavior of the two NBDs in the course of the MD simulation. By contrast, the NBDs in the wild-type are significantly more asymmetric (0.15 nm RMSD). For interpreting this result, one has to consider that completely symmetric behavior cannot be expected, because different instantaneous deviations of NBD1 and NBD2 even from identical average structures of the two would, after pairwise fitting of corresponding MD time frames, yield a nonzero RMSD. In addition, insufficient sampling can also contribute to apparent, transient asymmetry, as reported for the homodimeric ABC exporter Sav1866 (37).

Indeed, the RMSD between the average structures obtained from our MD simulations is smaller (Fig. 2 *B*, *vertical lines*). However, it is 1) larger than in the x-ray structure, and 2) larger in the wild-type than in the disulfide mutant. In addition, sampling limitations should be equally present in both wt and mutant, and thus the observed differences are meaningful. Asymmetric conformations of homodimeric ABC transporters have also been shown experimentally for MsbA (81). Finally, we note that in our simulations of the wild-type, Mg^{2+} is coordinated by the catalytic E159 in NBD2, but not in NBD1 (see Fig. S3), which could thus

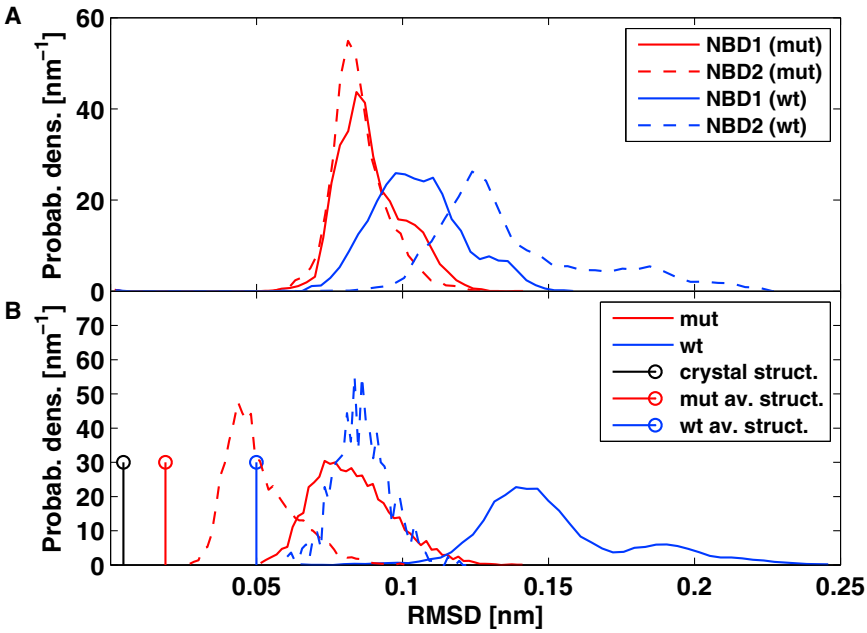

FIGURE 2 Distribution of RMSD of NBD1 and NBD2, obtained from combined data of all simulations (Table 1). For each NBD, the all-atom RMSD (including side-chain atoms) with respect to the starting structure was calculated. (*A*) RMSD from starting structure. (*B*) RMSD of NBD2 with respect to NBD1. The distributions show the instantaneous NBD1/NBD2 asymmetry during the MD (*solid lines*, all atoms; *dashed lines*, only Cα-atoms). The vertical lines indicate the RMSD in the x-ray structure (*black*) and between the average structures obtained from the MD (*red* and *blue* for E159Q/N162C mutant and wild-type, respectively). Only Cα-atoms were considered for calculating the RMSD between the average structures. To see this figure in color, go online.

contribute to the observed asymmetry. Therefore, we carried out an additional 1000-ns control simulation of the wild-type with the same Mg^{2+} coordination in both NBDs (by S40, Q80, and E159, in addition to ATP phosphates). This simulation yielded a similar asymmetry, with a mean all-atom RMSD of NBD2 with respect to NBD1 of 0.14 nm, comparable to the results shown in Fig. 2 *B*. Although coordination of Mg^{2+} by the catalytic glutamate was also observed in MD simulations of Sav1866 (37), further studies are necessary to explore whether the catalytic glutamate can coordinate Mg^{2+}. In summary, we conclude that removing the C162-C162 disulfide bond loosens the coupling between NBD1 and NBD2 and leads to a higher degree of transient structural asymmetry. Although not explicitly studied here, we speculate that this could be linked to asymmetric ATP hydrolysis in the two NBDs.

Next, to more closely analyze the observed asymmetric structural dynamics, we calculated the Cα root mean-square fluctuations (RMSFs) of each residue in BtuD around its average position (Fig. 3). To compare wild-type and mutant fluctuations, Fig. 3 shows the relative increase in RMSF with respect to the E159Q/N162C mutant, $\Delta RMSF = (RMSF_{wt}\text{-}RMSF_{mut})/RMSF_{mut}$. Overall, the fluctuations of the individual residues are increased in the wild-type as compared to the disulfide mutant. Especially the motifs responsible for ATP binding and hydrolysis are affected (highlighted in Fig. 3). As shown in Table 2, this increase in fluctuations is more pronounced for NBD2 than for NBD1, consistent with the results discussed above. Notable is the pronounced fluctuation of the H191 switch region,

TABLE 2 Cα-RMSF Increase Relative to E159Q/N162C Disulfide Mutant, Averaged over Residues Belonging to the Respective Motifs

Motif	Increase in NBD1 (%)	Increase in NBD2 (%)
Walker A	14	25
Walker B	37	8
Q-loop	42	17
Switch	31	94
LSGGE	20	47
D-loop	13	19

with an RMSF increase of 31 and 94% in NBD1 and NBD2, respectively. Closer inspection revealed that this increase is due to a flip of H191 between two states. In the starting (x-ray crystal) structure, the H191 side chain is hydrogen-bonded via its N_ε-H to the ATP γ-phosphate. We observed that this hydrogen bond can break (Fig. 4 *A*), which occurred more frequently in the wild-type than in the E159Q/N162C mutant. For wt NBD2, the H191–ATP hydrogen bond was broken in four out of five simulations, whereas for NBD1 the breakage was observed in only two out of five simulations. Once the hydrogen bond is broken, the H191 side chain has a substantially increased mobility and can even completely flip to an outward conformation in which it is oriented away from the ATP. By contrast, for the disulfide mutant, this H191 flip was much less pronounced: it was not seen in any of the five simulations in NBD2, and in two out of five cases for NBD1. The outward-pointing conformation of H191 seen in our simulations of the ATP-bound wt is similar to the conformation

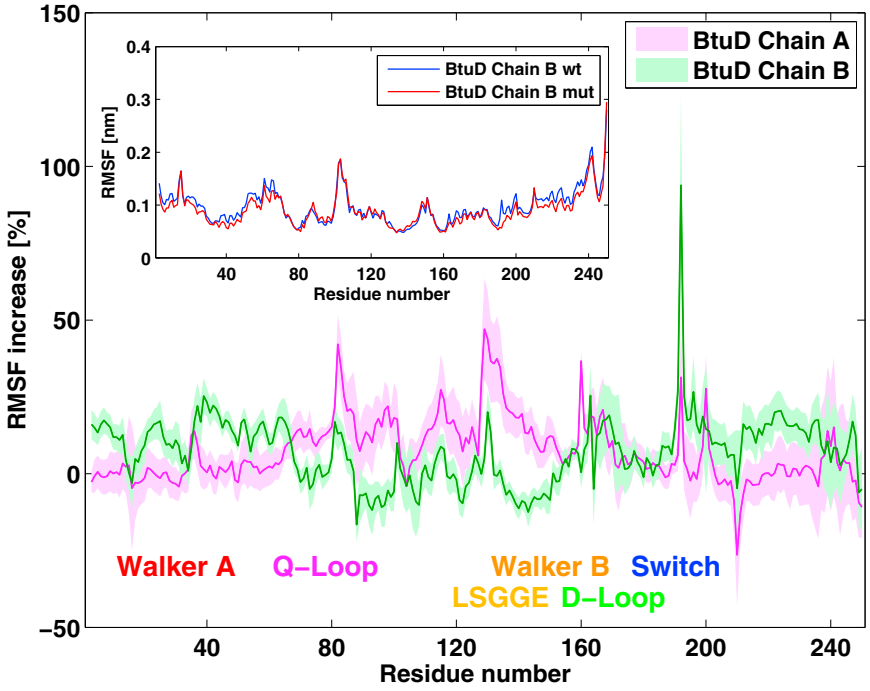

FIGURE 3 Relative increase in Cα-RMSF with respect to E159Q/N162C mutant. (*Shaded area*) Statistical uncertainty. (*Inset*) Absolute RMSF for chain B of wt (*blue*) and mutant (*red*) BtuD. To see this figure in color, go online.

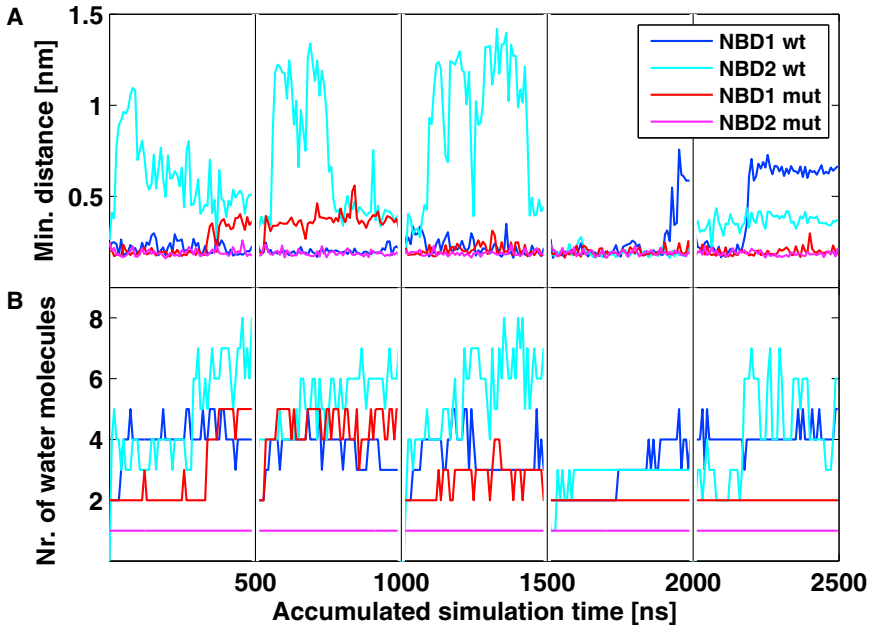

FIGURE 4 Minimum distance between any H191 side-chain atom to any γ-phosphate atom in the course of the five independent MD simulations (*A*) and number of water molecules in the corresponding NBDs (*B*). To see this figure in color, go online.

of H191 in the x-ray crystal structures of nucleotide-free BtuCD-F (11) and vanadate-bound BtuCD (10).

As an additional check, we also carried out five independent 500-ns MD simulations with doubly protonated H191 (see Fig. S2). These simulations show a similar conformational dynamics of H191, including the transitions to an outward-pointing conformation in NBD2. Fig. 4 *B* and Table 3 show that the H191 flip correlates with the number of water molecules that are in close proximity to the γ-phosphate. In mutant NBD2, where the hydrogen bond between H191 and the γ-phosphate is never broken, a single water molecule is within 0.5 nm of the P_γ atom. This water is also coordinating Mg^{2+} and does not exchange with other (bulk) waters on the simulation timescale (see Fig. S3 for a more detailed analysis of the local environment of the hexa-coordinated Mg^{2+} ion). In mutant NBD1, an average of 2.8 water molecules are close to P_γ. In this case, several different water molecules enter and leave the ATP binding pocket region during the simulations (Table 3). In the wild-type, the average water occupancies are 3.6 and 4.4 for NBD1 and NBD2, respectively, and again several different water molecules are involved. Thus, both the average occupancy and the dynamic exchange of water molecules between the ATP binding pocket and the bulk are linked to the conformational switch of H191, which acts as a gatekeeper for water access to the ATP γ-phosphate. We note that our findings do not contradict a linchpin-like (82) function of the histidine in the inward-pointing conformation, holding together the γ-phosphate and the catalytic glutamate during hydrolytic water attack. Whether and how the observed conformational dynamics of the highly conserved histidine residue plays a role in the ATP hydrolysis mechanism, and/or the release of hydrolysis products, is an interesting question but beyond the scope of this work.

TABLE 3 Water Molecules in the NBDs

System	No. of H_2O	τ (ns)	Occupancy
NBD1 mut	18	77	2.8
NBD2 mut	1	>500	1.0
NBD1 wt	18	100	3.6
NBD2 wt	249	9	4.4

A water molecule was counted if it was within 0.5 nm of the ATP P_γ atom. The table contains the number of different water molecules in the vicinity of P_γ during the 500-ns simulations, their mean residence time, and the average number of water molecules (occupancy).

Configurational entropy

Our above analysis revealed that the ATP-bound wild-type and E159Q/N162C disulfide mutant differ in terms of their fluctuations at the level of individual residues, suggesting different configurational entropies. In the following, we quantitatively investigate the thermodynamic implications linked to the introduction of the C162 disulfide bond, as well as of ATP binding, by comparing the configurational entropies of wild-type and mutant BtuCD-F in the ATP-bound state, and of wt BtuCD-F in the apo state. Our entropy calculations are based on the quasi-harmonic approximation as formulated by Schlitter (70), which links the atomic fluctuations to configurational entropy; see Materials and Methods. For proper statistics, we analyzed a concatenated data set consisting of all independent simulations (2500 ns sampling for each system). Fig. 5 shows the time evolution of the configurational entropy difference with respect to the ATP-bound wild-type, $\Delta S = S_X - S_{\text{wt-ATP}}$, where X denotes either the E159Q/N162C mutant (*solid lines*) or the apo* wild-type (*dashed*

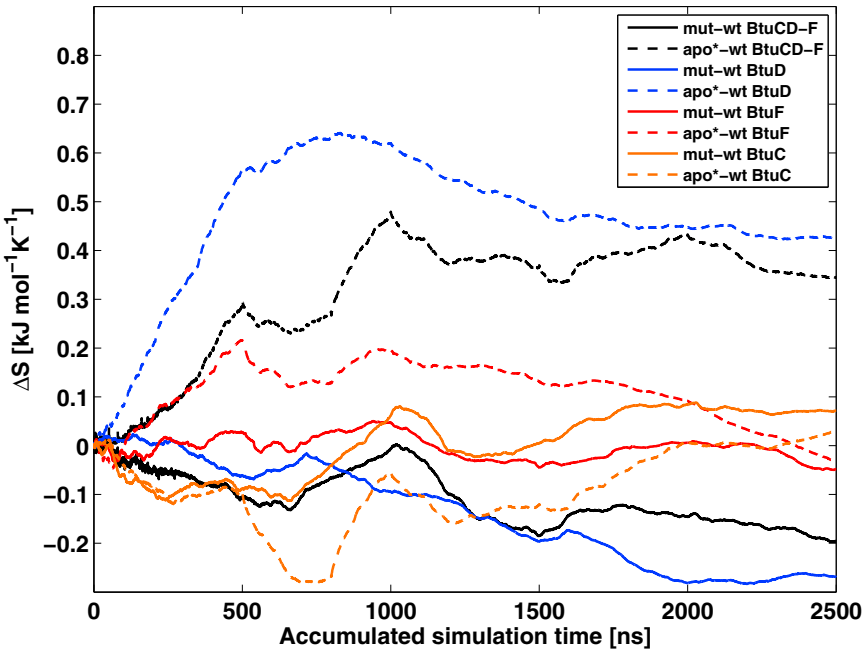

FIGURE 5 Entropy differences with respect to the ATP-bound wild-type. (*Solid lines*) E159Q/N162C disulfide mutant. (*Dashed lines*) apo* wild-type. To see this figure in color, go online.

lines). The corresponding entropy differences for the actual apo (instead of apo*) state are shown in Fig. S4 and agree closely with the ones in Fig. 5, showing that initializing the simulations from a conformationally excited apo* state does not affect the results. The entropy differences are reasonably converged after 2500 ns accumulated sampling and reveal that S_{config} of mutant BtuCD-F is lower than of the wild-type ($\Delta S = -0.20$ kJ mol^{-1} K^{-1}, *black solid line*). By contrast, removing ATP from the wild-type leads to an entropy increase of the whole transporter, of ~0.34 kJ mol^{-1} K^{-1} (*black dashed line*). In agreement with the RMSF analysis described above, the entropy changes can be attributed to the ATP binding cassette (BtuD, *blue lines*), whereas ΔS is close to zero for BtuC and *F*. For ATP binding, this entropy increase thus needs to be overcompensated, e.g., by binding energy and contributions due to solvent reorganization.

Mechanical stress on the disulfide bond

Our entropy analysis revealed that the disulfide bond in the E159Q/N162C mutant lowers the entropy of the transporter, especially in the NBDs. This entropy difference corresponds to a contribution of $T\Delta S$ to work that needs to be accomplished by the disulfide bridge, strongly suggesting a mechanically stressed S-S bond. Fig. 6 *A* shows that indeed, a substantial force acts on the C162-C162 bond. The disulfide bond switches between two distinct states, which correspond to repulsive (positive) and attractive (negative) forces. These two force states peak at +116 pN (occupation 90%) and −179 pN (occupation 10%), respectively, with frequent transitions between the two states (Fig. 6 *B*). Such a substantial force on the S-S bond can alter the reactivity of the disulfide (83–88). For comparison, the force on the C183-C259 disulfide bond in the BtuF domain is much smaller (~55 pN) and does not show a similar two-state behavior. In the major, repulsive force state the C162-C162 disulfide bond is under strain (i.e., it is stretched), whereas in the minor state it is compressed. Closer analysis of all dihedrals in the vicinity of the S-S bond revealed that the dihedral angle across the S-S bond, Cβ-S-S-Cβ, is the key link between the force and the structural rearrangement of the disulfide linkage (Fig. 6 *B*, *inset*). In addition, the stress is also evident from the strained C-S-S angles, which are on average 106.0° as compared to an equilibrium angle of 103.7° in the force field.

Force propagation pathways

The above analysis focused on the mechanical stress upon the engineered C162-C162 disulfide bond. However, because this S-S bond is of course absent in the wild-type, we aimed at characterizing the consequences of removing this disulfide linkage in terms of interresidual forces. Therefore, we performed FDA (see Materials and Methods), focusing on the differences between the E159Q/N162C disulfide mutant and the wild-type, and how exactly the force differences are distributed over the protein structure. Fig. 7 shows a mapping of the force difference networks onto the transporter. These networks provide the basis for the long-range coupling between conformational changes in the NBDs and the TMDs. The largest force differences are observed at the NBD dimer interface and in the vicinity of the ATP binding site. That was expected, because the N162C and E159Q mutations are located in that part of the structure. Furthermore, FDA

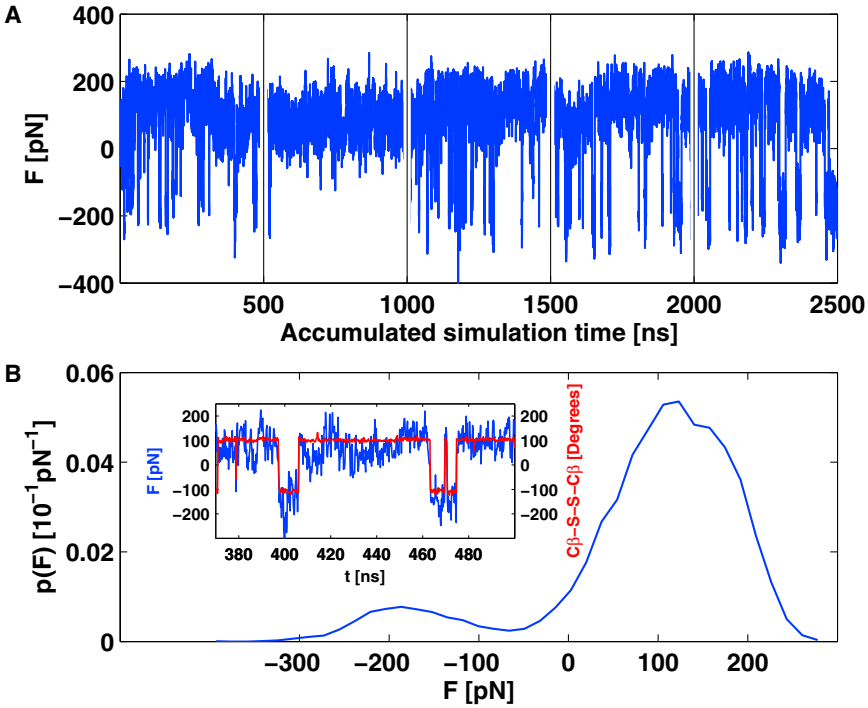

FIGURE 6 Force acting on the C162-C162 disulfide bond (*A*) and the corresponding distribution (*B*). The force and the dihedral angle across the S-S linkage are correlated (*inset*). The time traces shown are 200 ps moving averages. To see this figure in color, go online.

reveals that force differences are transmitted to the coupling helix and propagated through the TMD core toward the periplasmic side of the transporter. Interestingly, unlike in the NBDs (see below), force propagation through the core of the TMDs occurs predominantly along the individual helices, especially the TM5 gating helices, and does not involve many residue pairs across the TMD dimer interface (see Fig. S5). We speculate that this renders the mechanism robust in two regards: first, with respect to the presence of substrate, which could otherwise perturb the force transmission pathway by binding at the dimer interface; and second, mutations in the TM helices would be tolerated (as long as they do not disrupt the helix), because the pathway proceeds along the backbone hydrogen bonds.

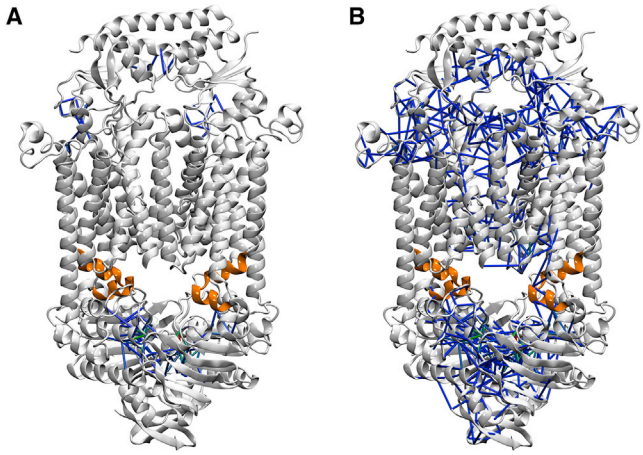

FIGURE 7 Force difference network. Force differences larger than 100 pN (*A*) and 50 pN (*B*) are shown as cylinders and color-coded according to magnitude (from *blue*, small ΔF, to *red*, large ΔF). The L2 coupling helix motif is shown in orange. Force differences are transmitted from the NBD interface via the coupling helix through the core of BtuC toward BtuF. To see this figure in color, go online.

The force analysis shown in Fig. 7 visualizes the mechanics underlying the conformational coupling mechanism of BtuCD-F in a clear manner. This may be considered surprising, given that we analyzed force differences between two ATP-bound states (disulfide mutant versus wild-type), whereas ABC transporters are driven by ATP binding and hydrolysis. Thus, from a physiological perspective, it might be more meaningful to consider the ATP-bound and -unbound states instead. Therefore, we have repeated the above analysis and calculated the force differences between the ATP-bound and -free wild-type. The results are qualitatively similar to the force differences between the disulfide mutant and the wild-type (see Fig. S6). In addition, similar results were obtained for the apo and apo* states. This indicates that the transmission pathways, as probed by the release of the stressed disulfide bridge upon converting the mutant to the wild-type, report on the same mechanical couplings as ATP binding/unbinding does.

Next, to more closely analyze which residues play a key role in the observed transmission networks, we focused on residue-residue force differences larger than 100 pN in BtuD. This analysis revealed two main networks that are interconnected, one from the ATP binding site toward the coupling helix (network 1), and the other across the NBD dimer interface (network 2). Network 1 is shown in Fig. 8 and the forces are listed in Table S1 in the Supporting Material. Originating from S40 (Walker A) and E/Q159

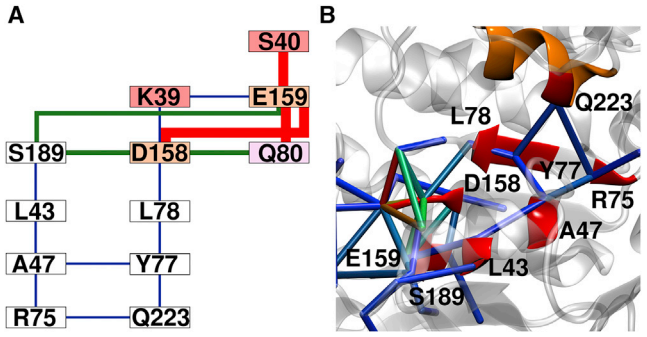

FIGURE 8 Force difference network from the ATP binding site to the coupling helix (network 1). (*A*) Residues involved in this network. (*Red thick lines*) $\Delta F > 700$ pN; (*green lines*) $\Delta F > 300$ pN; (*thin blue lines*) $\Delta F > 100$ pN. (*B*) Zoom on NBD2 with mapping of the force differences. Residues that are part of the network are highlighted in red. To see this figure in color, go online.

(Walker B) at the ATP binding site, force differences are transmitted over two pathways toward Q223 in the coupling helix. The first pathway involves S189, L43, A47, and R75, whereas the second one proceeds via D158, L78, and Y77. These two pathways are connected (A47-Y77).

Network 2 (Fig. 9) highlights the changes that occur at the NBD interface. Upon conversion of the disulfide mutant to the wild-type, pairwise residue-residue forces decrease on average (see Table S2), i.e., get less repulsive (or even more attractive, as for S163-E/Q159). These relaxation processes mainly take place within the LSGGE motif, between LSGGE and Walker A residues, and between D-loop residue D165 and the H191 switch. Thus, the mechanical stress associated with the close contact of the two NBDs, enforced by the C162-C162 disulfide bond, is released in the wt, in line with increased average distances between the residues involved in the NBD1/2 interface and the larger fluctuations (see above). These identified networks partly comprise residues of the motifs essential for ATP binding and hydrolysis (colored in

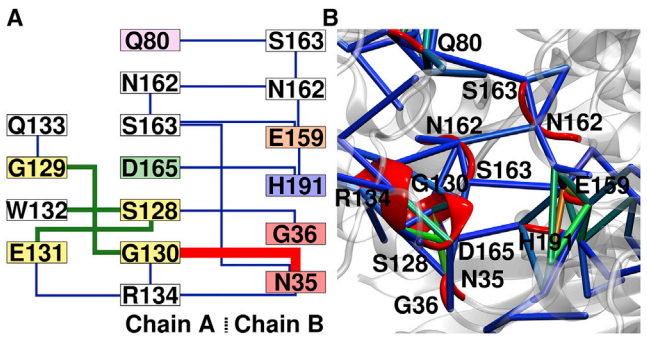

FIGURE 9 Force difference network across the NBD dimer interface (network 2). (*A*) Residues involved in this network. (*Red thick lines*) $\Delta F > 700$ pN; (*green lines*) $\Delta F > 300$ pN; (*thin blue lines*) $\Delta F > 100$ pN. (*B*) Zoom on NBD2 with mapping of the force differences. Residues that are part of the network are highlighted in red. To see this figure in color, go online.

Figs. 8 *A* and 9 *A*), but also other residues that are conserved as well (see below).

In addition to the magnitude of the force differences between the residues, the number of links that each residue establishes to other residues in the force network might also be of importance. For example, in an idealized, hypothetical network in which all pairwise force differences are identical, those knots that are connected to a large number of neighbors would be central for overall transmission. The connectivity analysis in Fig. S7 shows a distinct pattern throughout the sequence of BtuD. This pattern agrees with the previous analysis of the strongest residue-residue force differences, indicating that both the number of connections and the strength of the connections provide a congruent picture. In addition, the results obtained for different ΔF thresholds are consistent, indicating that our findings are statistically robust. In this context, we point out that due to the large fluctuations of the forces, microsecond timescale simulations were required for obtaining statistically meaningful results (see Fig. S8 for a closer analysis of statistical noise).

Our simulations clearly visualize the mechanical coupling mechanism. Direct experimental validation is difficult, though, because it is very challenging to measure individual residue-residue forces. However, sequence alignment (Fig. S9) shows that the residues involved in the identified networks are highly conserved between different bacteriae, strongly supporting the identified force transmission pathways. Notably, not only are the motifs essential for nucleotide binding and hydrolysis conserved, but also virtually all residues of the force networks. Out of the 22 residues involved in the force propagation networks, 18 are strictly conserved and 3 show high similarity. Close inspection revealed that the only nonconserved residue, S189, transmits forces mainly via the backbone, consistent with the observation that S189 can be replaced by another small amino acid such as cysteine or alanine. In summary, based on these findings, we propose that mutation of the network residues will affect the function of the transporter, a prediction that can be tested experimentally.

CONCLUSIONS

We investigated the structural dynamics and conformational coupling mechanism of the ABC transporter BtuCD-F by means of atomistic MD simulations. In addition to the wild-type transporter in the ATP-bound and -free states, we considered the E159Q/N162C mutant with an engineered S-S bond between the two NBDs, which was introduced for crystallization of the nucleotide-bound states (13,14). Our simulations reveal that the wild-type transporter that lacks the C162-C162 disulfide bond undergoes increased fluctuations, which are localized especially in those NBD motifs that are essential for ATP binding and hydrolysis. Furthermore, the two NBDs are slightly asymmetric, both

in terms of their structure and in their dynamic fluctuations. The H191 switch is flexible in the wild-type and can adopt two distinct conformations even in the presence of ATP—an inward-pointing state in which the H191 side chain is hydrogen-bonded to ATP, and an outward-pointing state that is similar to the conformation seen in other x-ray crystal structures (10,11).

Thus, in addition to its linchpin function (82), H191 acts as a gatekeeper that regulates water access to the ATP γ-phosphate, with possible mechanistic implications. Configurational entropy analysis revealed how the engineered C162 disulfide bond reduces conformational fluctuations in the NBDs, thus leading to an entropic force acting on the S-S bond. Release of this entropic spring, as probed by the simulations of the wild-type, in combination with a spatially resolved analysis of the interresidue forces, enabled mapping of distinct pathways along which force is propagated from the NBDs via the coupling helix to the TMDs. The residues involved in these identified networks are highly conserved, suggesting that they play a functional role. Highly similar pathways were found when analyzing the corresponding force differences between ATP-bound and -free wild-type proteins (instead of between ATP-bound wild-type and E159Q/N162C disulfide mutant). Hence, breaking the S-S bond reports on the same structural dynamics and conformational couplings as ATP unbinding, a result that can be attributed to the similar location of the S-S bond and the ATP binding site near the NBD dimer interface.

From a somewhat more general perspective, ABC transporters can be understood as molecular machines whose functional working cycle is based on converting the chemical energy stored in ATP into mechanical work. The forces generated in the ATP binding site in the NBDs are transmitted through the protein structure toward the TMDs, which ultimately undergo large-scale conformational motions that lead to the transport of substrate. Hence, analyzing the forces between the individual elements of the molecular machine can sensitively probe these mechanical couplings, as shown in this work; although we did not explicitly sample the conformational changes between the inward- and outward-facing states, which take place on much slower timescales. In addition, a complete understanding of the transport mechanism requires taking several other factors into account, such as ATP binding, hydrolysis, and product release (which we included in this work only in an approximate, ad hoc manner by instantaneous removal of ATP) and, importantly, to explicitly include a substrate molecule. In addition to the ongoing efforts to obtain high-resolution x-ray crystal structures, MD simulations will likely play a key role in addressing these formidable challenges, especially when combined with enhanced sampling techniques and the calculation of free energy profiles along suitably chosen reaction coordinates, taking ATP binding and hydrolysis, as well as large-scale conformational changes, into account.

SUPPORTING MATERIAL

Nine figures and two tables are available at http://www.biophysj.org/biophysj/supplemental/S0006-3495(16)30230-2.

AUTHOR CONTRIBUTIONS

M.P. designed and performed research, contributed analysis tools, analyzed data, prepared the figures and tables, and co-wrote the article; and L.V.S. designed research, analyzed data, and wrote the article.

ACKNOWLEDGMENTS

We thank Frauke Gräter, Maxime Louet, and Beifei Zhou for help with FDA; Enrica Bordignon, Eckhard Hofmann, and Benesh Joseph for insightful discussions; Hendrik Göddeke for carrying out additional control simulations; and Olivier Fisette for help with sequence alignment.

This work was funded by the Deutsche Forschungsgemeinschaft through Cluster of Excellence RESOLV (EXC 1069), SFB 807 (Transport and Communication across Biological Membranes), and the Emmy Noether grant to L.V.S.

REFERENCES

1. Hollenstein, K., R. J. Dawson, and K. P. Locher. 2007. Structure and mechanism of ABC transporter proteins. *Curr. Opin. Struct. Biol.* 17:412–418.
2. Davidson, A. L., and P. C. Maloney. 2007. ABC transporters: how small machines do a big job. *Trends Microbiol.* 15:448–455.
3. Davidson, A. L., E. Dassa, …, J. Chen. 2008. Structure, function, and evolution of bacterial ATP-binding cassette systems. *Microbiol. Mol. Biol. Rev.* 72:317–364.
4. Rees, D. C., E. Johnson, and O. Lewinson. 2009. ABC transporters: the power to change. *Nat. Rev. Mol. Cell Biol.* 10:218–227.
5. Parcej, D., and R. Tampé. 2010. ABC proteins in antigen translocation and viral inhibition. *Nat. Chem. Biol.* 6:572–580.
6. ter Beek, J., A. Guskov, and D. J. Slotboom. 2014. Structural diversity of ABC transporters. *J. Gen. Physiol.* 143:419–435.
7. Silverton, L., M. Dean, and K. Moitra. 2011. Variation and evolution of the ABC transporter genes ABCB1, ABCC1, ABCG2, ABCG5 and ABCG8: implication for pharmacogenetics and disease. *Drug Metabol. Drug Interact.* 26:169–179.
8. Krulwich, T. A., O. Lewinson, …, E. Bibi. 2005. Do physiological roles foster persistence of drug/multidrug-efflux transporters? A case study. *Nat. Rev. Microbiol.* 3:566–572.
9. Ambudkar, S. V., C. Kimchi-Sarfaty, …, M. M. Gottesman. 2003. P-glycoprotein: from genomics to mechanism. *Oncogene.* 22:7468–7485.
10. Locher, K. P., A. T. Lee, and D. C. Rees. 2002. The *E. coli* BtuCD structure: a framework for ABC transporter architecture and mechanism. *Science.* 296:1091–1098.
11. Hvorup, R. N., B. A. Goetz, …, K. P. Locher. 2007. Asymmetry in the structure of the ABC transporter-binding protein complex BtuCD-BtuF. *Science.* 317:1387–1390.
12. Korkhov, V. M., S. A. Mireku, …, K. P. Locher. 2012. Asymmetric states of vitamin B12 transporter BtuCD are not discriminated by its cognate substrate binding protein BtuF. *FEBS Lett.* 586:972–976.
13. Korkhov, V. M., S. A. Mireku, and K. P. Locher. 2012. Structure of AMP-PNP-bound vitamin B12 transporter BtuCD-F. *Nature.* 490:367–372.
14. Korkhov, V. M., S. A. Mireku, …, K. P. Locher. 2014. Structure of AMP-PNP-bound BtuCD and mechanism of ATP-powered vitamin B12 transport by BtuCD-F. *Nat. Struct. Mol. Biol.* 21:1097–1099.

15. Lewinson, O., A. T. Lee, …, D. C. Rees. 2010. A distinct mechanism for the ABC transporter BtuCD-BtuF revealed by the dynamics of complex formation. *Nat. Struct. Mol. Biol.* 17:332–338.
16. Pinkett, H. W., A. T. Lee, …, D. C. Rees. 2007. An inward-facing conformation of a putative metal-chelate-type ABC transporter. *Science.* 315:373–377.
17. Borths, E. L., B. Poolman, …, D. C. Rees. 2005. In vitro functional characterization of BtuCD-F, the *Escherichia coli* ABC transporter for vitamin B12 uptake. *Biochemistry.* 44:16301–16309.
18. Klein, J. S., and O. Lewinson. 2011. Bacterial ATP-driven transporters of transition metals: physiological roles, mechanisms of action, and roles in bacterial virulence. *Metallomics.* 3:1098–1108.
19. Goetz, B. A., E. Perozo, and K. P. Locher. 2009. Distinct gate conformations of the ABC transporter BtuCD revealed by electron spin resonance spectroscopy and chemical cross-linking. *FEBS Lett.* 583:266–270.
20. Joseph, B., G. Jeschke, …, E. Bordignon. 2011. Transmembrane gate movements in the type II ATP-binding cassette (ABC) importer BtuCD-F during nucleotide cycle. *J. Biol. Chem.* 286:41008–41017.
21. Joseph, B., V. M. Korkhov, …, E. Bordignon. 2014. Conformational cycle of the vitamin B12 ABC importer in liposomes detected by double electron-electron resonance (DEER). *J. Biol. Chem.* 289:3176–3185.
22. Lindahl, E., and M. S. Sansom. 2008. Membrane proteins: molecular dynamics simulations. *Curr. Opin. Struct. Biol.* 18:425–431.
23. Khalili-Araghi, F., J. Gumbart, …, K. Schulten. 2009. Molecular dynamics simulations of membrane channels and transporters. *Curr. Opin. Struct. Biol.* 19:128–137.
24. Jones, P. M., and A. M. George. 2002. Mechanism of ABC transporters: a molecular dynamics simulation of a well characterized nucleotide-binding subunit. *Proc. Natl. Acad. Sci. USA.* 99:12639–12644.
25. Campbell, J. D., S. S. Deol, …, M. S. P. Sansom. 2004. Nucleotide-dependent conformational changes in HisP: molecular dynamics simulations of an ABC transporter nucleotide-binding domain. *Biophys. J.* 87:3703–3715.
26. Campbell, J. D., and M. S. P. Sansom. 2005. Nucleotide binding to the homodimeric MJ0796 protein: a computational study of a prokaryotic ABC transporter NBD dimer. *FEBS Lett.* 579:4193–4199.
27. Oloo, E. O., E. Y. Fung, and D. P. Tieleman. 2006. The dynamics of the MgATP-driven closure of MalK, the energy-transducing subunit of the maltose ABC transporter. *J. Biol. Chem.* 281:28397–28407.
28. Jones, P. M., and A. M. George. 2007. Nucleotide-dependent allostery within the ABC transporter ATP-binding cassette: a computational study of the MJ0796 dimer. *J. Biol. Chem.* 282:22793–22803.
29. Wen, P.-C., and E. Tajkhorshid. 2008. Dimer opening of the nucleotide binding domains of ABC transporters after ATP hydrolysis. *Biophys. J.* 95:5100–5110.
30. Newstead, S., P. W. Fowler, …, S. Iwata. 2009. Insights into how nucleotide-binding domains power ABC transport. *Structure.* 17:1213–1222.
31. Jones, P. M., and A. M. George. 2009. Opening of the ADP-bound active site in the ABC transporter ATPase dimer: evidence for a constant contact, alternating sites model for the catalytic cycle. *Proteins.* 75:387–396.
32. Oliveira, A. S. F., A. M. Baptista, and C. M. Soares. 2010. Insights into the molecular mechanism of an ABC transporter: conformational changes in the NBD dimer of MJ0796. *J. Phys. Chem. B.* 114:5486–5496.
33. Jones, P. M., and A. M. George. 2011. Molecular-dynamics simulations of the ATP/apo state of a multidrug ATP-binding cassette transporter provide a structural and mechanistic basis for the asymmetric occluded state. *Biophys. J.* 100:3025–3034.
34. Jones, P. M., and A. M. George. 2012. Role of the D-loops in allosteric control of ATP hydrolysis in an ABC transporter. *J. Phys. Chem. A.* 116:3004–3013.
35. George, A. M., and P. M. Jones. 2013. An asymmetric post-hydrolysis state of the ABC transporter ATPase dimer. *PLoS One.* 8:e59854.
36. Becker, J.-P., F. van Bambeke, …, M. Prévost. 2010. Dynamics and structural changes induced by ATP binding in SAV1866, a bacterial ABC exporter. *J. Phys. Chem. B.* 114:15948–15957.
37. Aittoniemi, J., H. de Wet, …, M. S. Sansom. 2010. Asymmetric switching in a homodimeric ABC transporter: a simulation study. *PLOS Comput. Biol.* 6:e1000762.
38. Weng, J.-W., K.-N. Fan, and W.-N. Wang. 2010. The conformational transition pathway of ATP binding cassette transporter MsbA revealed by atomistic simulations. *J. Biol. Chem.* 285:3053–3063.
39. Wen, P.-C., and E. Tajkhorshid. 2011. Conformational coupling of the nucleotide-binding and the transmembrane domains in ABC transporters. *Biophys. J.* 101:680–690.
40. Oliveira, A. S., A. M. Baptista, and C. M. Soares. 2011. Conformational changes induced by ATP-hydrolysis in an ABC transporter: a molecular dynamics study of the Sav1866 exporter. *Proteins.* 79:1977–1990.
41. O'Mara, M. L., and A. E. Mark. 2012. The effect of environment on the structure of a membrane protein: P-glycoprotein under physiological conditions. *J. Chem. Theory Comput.* 8:3964–3976.
42. St-Pierre, J.-F., A. Bunker, …, N. Mousseau. 2012. Molecular dynamics simulations of the bacterial ABC transporter SAV1866 in the closed form. *J. Phys. Chem. B.* 116:2934–2942.
43. Moradi, M., and E. Tajkhorshid. 2013. Mechanistic picture for conformational transition of a membrane transporter at atomic resolution. *Proc. Natl. Acad. Sci. USA.* 110:18916–18921.
44. Wen, P.-C., B. Verhalen, …, E. Tajkhorshid. 2013. On the origin of large flexibility of P-glycoprotein in the inward-facing state. *J. Biol. Chem.* 288:19211–19220.
45. Shintre, C. A., A. C. W. Pike, …, E. P. Carpenter. 2013. Structures of ABCB10, a human ATP-binding cassette transporter in apo- and nucleotide-bound states. *Proc. Natl. Acad. Sci. USA.* 110:9710–9715.
46. O'Mara, M. L., and A. E. Mark. 2014. Structural characterization of two metastable ATP-bound states of P-glycoprotein. *PLoS One.* 9:e91916.
47. Gu, R.-X., V. Corradi, …, D. P. Tieleman. 2015. Conformational changes of the antibacterial peptide ATP binding cassette transporter McjD revealed by molecular dynamics simulations. *Biochemistry.* 54:5989–5998.
48. Oloo, E. O., and D. P. Tieleman. 2004. Conformational transitions induced by the binding of MgATP to the vitamin B12 ATP-binding cassette (ABC) transporter BtuCD. *J. Biol. Chem.* 279:45013–45019.
49. Sonne, J., C. Kandt, …, D. P. Tieleman. 2007. Simulation of the coupling between nucleotide binding and transmembrane domains in the ATP binding cassette transporter BtuCD. *Biophys. J.* 92:2727–2734.
50. Ivetac, A., J. D. Campbell, and M. S. Sansom. 2007. Dynamics and function in a bacterial ABC transporter: simulation studies of the BtuCDF system and its components. *Biochemistry.* 46:2767–2778.
51. Kandt, C., and D. P. Tieleman. 2010. Holo-BtuF stabilizes the open conformation of the vitamin B12 ABC transporter BtuCD. *Proteins.* 78:738–753.
52. Weng, J., K. Fan, and W. Wang. 2012. The conformational transition pathways of ATP-binding cassette transporter BtuCD revealed by targeted molecular dynamics simulation. *PLoS One.* 7:e30465.
53. Hess, B., C. Kutzner, …, E. Lindahl. 2008. GROMACS 4: algorithms for highly efficient, load-balanced, and scalable molecular simulation. *J. Chem. Theory Comput.* 4:435–447.
54. Pronk, S., S. Páll, …, E. Lindahl. 2013. GROMACS 4.5: a high-throughput and highly parallel open source molecular simulation toolkit. *Bioinformatics.* 29:845–854.
55. Lomize, M. A., I. D. Pogozheva, …, A. L. Lomize. 2012. OPM database and PPM web server: resources for positioning of proteins in membranes. *Nucleic Acids Res.* 40:D370–D376.
56. Kandt, C., W. L. Ash, and D. P. Tieleman. 2007. Setting up and running molecular dynamics simulations of membrane proteins. *Methods.* 41:475–488.

57. Horn, H. W., W. C. Swope, …, T. Head-Gordon. 2004. Development of an improved four-site water model for biomolecular simulations: TIP4P-Ew. *J. Chem. Phys.* 120:9665–9678.

58. Lindorff-Larsen, K., S. Piana, …, D. E. Shaw. 2010. Improved side-chain torsion potentials for the Amber ff99SB protein force field. *Proteins.* 78:1950–1958.

59. Søndergaard, C. R., M. H. Olsson, …, J. H. Jensen. 2011. Improved treatment of ligands and coupling effects in empirical calculation and rationalization of pK_a values. *J. Chem. Theory Comput.* 7:2284–2295.

60. Olsson, M. H., C. R. Søndergaard, …, J. H. Jensen. 2011. PROPKA3: consistent treatment of internal and surface residues in empirical pK_a predictions. *J. Chem. Theory Comput.* 7:525–537.

61. Berger, O., O. Edholm, and F. Jähnig. 1997. Molecular dynamics simulations of a fluid bilayer of dipalmitoylphosphatidylcholine at full hydration, constant pressure, and constant temperature. *Biophys. J.* 72:2002–2013.

62. Cordomí, A., G. Caltabiano, and L. Pardo. 2012. Membrane protein simulations using AMBER force field and Berger lipid parameters. *J. Chem. Theory Comput.* 8:948–958.

63. Bachar, M., P. Brunelle, …, A. Rauk. 2004. Molecular dynamics simulation of a polyunsaturated lipid bilayer susceptible to lipid peroxidation. *J. Phys. Chem. B.* 108:7170–7179.

64. Meagher, K. L., L. T. Redman, and H. A. Carlson. 2003. Development of polyphosphate parameters for use with the AMBER force field. *J. Comput. Chem.* 24:1016–1025.

65. Darden, T., D. York, and L. Pedersen. 1993. Particle mesh Ewald: an N log(N) method for Ewald sums in large systems. *J. Chem. Phys.* 98:10089–10092.

66. Miyamoto, S., and P. A. Kollman. 1992. SETTLE: an analytical version of the SHAKE and RATTLE algorithm for rigid water models. *J. Comput. Chem.* 13:952–962.

67. Hess, B. 2008. P-LINCS: a parallel linear constraint solver for molecular simulation. *J. Chem. Theory Comput.* 4:116–122.

68. Feenstra, K. A., B. Hess, and H. J. Berendsen. 1999. Improving efficiency of large timescale molecular dynamics simulations of hydrogen-rich systems. *J. Comput. Chem.* 20:786–798.

69. Bussi, G., D. Donadio, and M. Parrinello. 2007. Canonical sampling through velocity rescaling. *J. Chem. Phys.* 126:014101.

70. Schlitter, J. 1993. Estimation of absolute and relative entropies of macromolecules using the covariance matrix. *Chem. Phys. Lett.* 215:617–621.

71. Baron, R., A. H. de Vries, …, W. F. van Gunsteren. 2006. Configurational entropies of lipids in pure and mixed bilayers from atomic-level and coarse-grained molecular dynamics simulations. *J. Phys. Chem. B.* 110:15602–15614.

72. Baron, R., A. H. de Vries, …, W. F. van Gunsteren. 2006. Comparison of atomic-level and coarse-grained models for liquid hydrocarbons from molecular dynamics configurational entropy estimates. *J. Phys. Chem. B.* 110:8464–8473.

73. Debnath, A., and L. V. Schäfer. 2015. Structure and dynamics of phospholipid nanodiscs from all-atom and coarse-grained simulations. *J. Phys. Chem. B.* 119:6991–7002.

74. Fisette, O., S. Wingbermühle, …, L. V. Schäfer. 2016. Molecular mechanism of peptide editing in the tapasin-MHC I complex. *Sci. Rep.* 6:19085.

75. Stacklies, W., M. C. Vega, …, F. Gräter. 2009. Mechanical network in titin immunoglobulin from force distribution analysis. *PLOS Comput. Biol.* 5:e1000306.

76. Stacklies, W., C. Seifert, and F. Graeter. 2011. Implementation of force distribution analysis for molecular dynamics simulations. *BMC Bioinformatics.* 12:101.

77. Seifert, C., and F. Gräter. 2013. Protein mechanics: how force regulates molecular function. *Biochim. Biophys. Acta.* 1830:4762–4768.

78. Palmai, Z., C. Seifert, …, E. Balog. 2014. An allosteric signaling pathway of human 3-phosphoglycerate kinase from force distribution analysis. *PLOS Comput. Biol.* 10:e1003444.

79. Louet, M., C. Seifert, …, F. Gräter. 2015. Dynamic allostery of the catabolite activator protein revealed by interatomic forces. *PLOS Comput. Biol.* 11:e1004358.

80. Costescu, B. I., and F. Gräter. 2013. Time-resolved force distribution analysis. *BMC Biophys.* 6:5.

81. Mittal, A., S. Böhm, …, M. A. Seeger. 2012. Asymmetry in the homodimeric ABC transporter MsbA recognized by a DARPin. *J. Biol. Chem.* 287:20395–20406.

82. Oldham, M. L., and J. Chen. 2011. Snapshots of the maltose transporter during ATP hydrolysis. *Proc. Natl. Acad. Sci. USA.* 108:15152–15156.

83. Liang, J., and J. M. Fernández. 2009. Mechanochemistry: one bond at a time. *ACS Nano.* 3:1628–1645.

84. Ribas-Arino, J., and D. Marx. 2012. Covalent mechanochemistry: theoretical concepts and computational tools with applications to molecular nanomechanics. *Chem. Rev.* 112:5412–5487.

85. Baldus, I. B., and F. Gräter. 2012. Mechanical force can fine-tune redox potentials of disulfide bonds. *Biophys. J.* 102:622–629.

86. Dopieralski, P., J. Ribas-Arino, …, D. Marx. 2013. The Janus-faced role of external forces in mechanochemical disulfide bond cleavage. *Nat. Chem.* 5:685–691.

87. Anjukandi, P., P. Dopieralski, …, D. Marx. 2014. The effect of tensile stress on the conformational free energy landscape of disulfide bonds. *PLoS One.* 9:e108812.

88. Zhou, B., I. B. Baldus, …, F. Gräter. 2014. Identification of allosteric disulfides from prestress analysis. *Biophys. J.* 107:672–681.